ELSEVIER

Soot concentration and primary particle size in swirl-stabilized non-premixed turbulent flames of ethylene and air☆

Sandipan Chatterjee, Ömer L. Gülder*

University of Toronto Institute for Aerospace Studies, 4925 Dufferin Street, Toronto, ON M3H 5T6, Canada

ARTICLE INFO

ABSTRACT

Turbulent non-premixed swirl-stabilized flames were investigated experimentally in a gas turbine model combustor with optical access. Velocity and soot concentration fields were measured for three levels of air flow for a fixed flow rate of ethylene as the fuel. Stereoscopic particle image velocimetry was used to get the three-dimensional velocity field data within the combustor. The time-averaged soot volume fractions and primary soot particles sizes were obtained using the laser induced incandescence technique. These two measurements were conducted separately, but under the identical experimental flow conditions. The velocity measurements showed a region of high velocity flow, sandwiched between inner and outer recirculation zones. The boundaries of the recirculation zones in all three cases displayed very high turbulence intensities. Most of the soot was found to be within the inner recirculation zone, and the regions having maximum time-averaged soot concentrations grew radially outward with axial height. The soot concentrations showed a strong dependence on air flow rate; a small increase in air flow rate caused a significant reduction in soot concentrations. The primary soot particle diameters inferred from laser induced incandescence measurements covered the range from 30 to 50 nm.

1. Introduction

Swirl-stabilized non-premixed combustion is the main building block of the most staged aviation gas turbine combustor architectures. The staged combustors deliver a delicate balance between various pollutant emissions and combustion performance indicators. In these architectures, instead of trying to achieve all pollutant and combustion performance goals in a single combustion zone, the practice is to spread these objectives over two or more combustion zones. In each zone, the aim is to achieve, and optimize if possible, certain performance objectives. Combustors designed to operate with staged combustion are widely used in conventional aviation and industrial gas turbine engines and are the subject of on-going research activities for further performance improvements and mitigation of pollutant emissions.

Most of the time in the first zone of the staged combustion systems, the flame is stabilized by the air swirl creating a recirculation to increase the residence time for combustion reactions [1,2]. The recirculating fluid is generally composed of hot unburned fuel, combustion products and chemically active radicals. Further, the high turbulence intensity that prevails in the recirculation zones, allows for a rapid transfer of heat and radicals to the in-flowing reactants from the recirculating fluids. This mechanism facilitates ignition of reactants with relative ease, and consequently, flame stabilization over a wide range of flow conditions becomes possible [2–6].

Formation of soot within the first zone of the staged combustors is unavoidable due to the mainly non-premixed nature of combustion. A significant portion of the soot that is formed within this zone in conventional gas turbine combustors is subsequently consumed by oxidation within the later stages of the combustion chamber. However, a small but important fraction avoids the oxidation process and is emitted as particulate matter from the engine exhaust. Apart from its potential impact on climate and human health [7], soot promotes radiative heat loss, leading to reduced engine thermal efficiency and increased heat load on the combustor components.

Understanding of the soot and NO_x processes in technically relevant combustors is central to the design of high-performance, low-emission gas turbine engines. Experiments performed on full-scale gas turbine combustors are not only expensive but are limited in scope of information that can be acquired due to measurement access limitations. This situation necessitates the development of numerical models capable of predicting flow fields and pollutant concentrations in gas turbine combustors. However, the current numerical schemes have not

achieved sufficient confidence to handle the complexities of swirling reacting flows in gas turbine combustors [8–10]. The growth of the numerical combustion modelling capabilities has been held back due to a shortage of validation suited experimental datasets with well-defined boundary conditions. To fulfil this demand for experimental data, there has been several recent experimental studies reporting detailed measurements in swirling/non-swirling, premixed/non-premixed, and atmospheric/high-pressure turbulent flames [8–26]. Various experimental techniques including high speed planar laser induced fluorescence (PLIF), stereoscopic particle image velocimetry (SPIV), and laser induced incandescence (LII) have been utilized for data acquisition.

Keck et al. [16] investigated swirling natural gas and air non-premixed flames in an industrial burner prototype. The temperature and species concentration distributions, derived from the Raman measurements, are utilized to characterize the three distinct regions of the flow field: inlet flow, inner recirculation zone (IRZ) and outer recirculation zone (ORZ). It is observed that near the common air-fuel nozzle exit plane, the flame reactions are suppressed by the high velocity inflow, and the shielding of the reactant mixtures from the hot recirculating products in the IRZ by the inflowing fuel stream. Hence, a partial premixing of the reactants occurs at the low axial locations, due to the high intensity turbulence prevailing in those regions. With increasing downstream locations, the flame reactions are seen to occur, and the corresponding causality between the turbulence-chemistry interactions and the thermo-chemical state of the flame is established.

In a similar study, Weigand et al. [20] discuss the velocity field, concentrations of OH and CH radicals, and the temperature distribution of a swirling methane-air diffusion flame in a gas turbine model combustor. A high velocity inlet flow in-between the two distinct recirculation zones is observed. The CH and OH concentration profiles show a thin, strongly wrinkled reaction zone in all the investigated flames. Weigand et al. [20] also report the occurrence of thermoacoustic oscillations in one of the investigated flames. Compared to the flames without thermo-acoustic oscillations, the flame with oscillations shows enhanced turbulent mixing rates of the cold reactants with the hot recirculating products, leading to accelerated reaction rates. The increase in the reaction rates produces a flame much shorter than the flames without thermo-acoustic oscillations. A detailed account of the turbulence-chemistry interactions in the flames studied by Weigand et al. [20] was reported by Meier et al. [21].

The topics of velocity field characterization, thermo-acoustics and coherent structure-flame interactions have been extensively investigated in model gas turbine combustors. However, soot measurements in swirling turbulent flames has not seen similar growth in the literature. Recently, Geigle et al. [11,12] reported soot measurements in turbulent non-premixed swirl flames of ethylene and air in a model gas turbine combustor. The SPIV and planar-LII measurements showed that most of the soot is spatially confined to the central recirculation zone of the flow field. The soot concentrations in the flow field showed a positive correlation with the global fuel-air equivalence ratio as well as the combustor chamber pressure. Further, the importance of the intermittency of soot events in the computation of the time-averaged value of the soot concentration was discussed. It should be emphasized here that velocity and scalar measurements in turbulent flames are problematic at high pressures. Zerbs et al. [25] explain that the steep temperature gradients in turbulent flames can cause considerable beam steering and large variation in the laser fluence across the laser sheet width. Further, the laser fluence variations can induce a considerable uncertainty in the computed soot volume fraction values. These impediments indicate that the uncertainty quantification of the velocity and scalar measurements can be a daunting task. For this reason, the experimental databases related to high pressure turbulent flames are growing slower than those of atmospheric flames [18,25].

The current study focuses on swirling non-premixed turbulent combustion of ethylene at atmospheric pressure in a gas turbine model
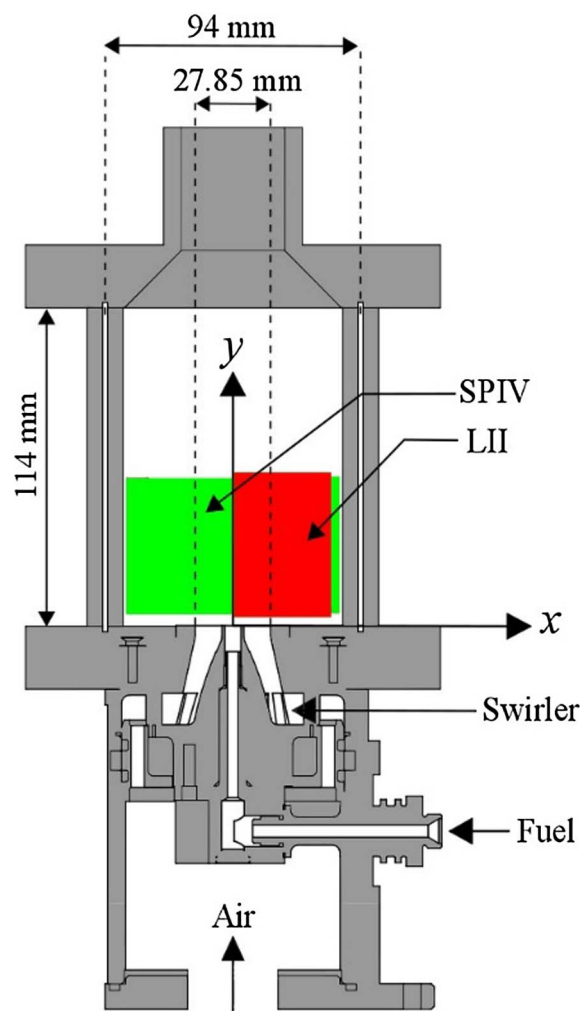

Fig. 1. Gas turbine model combustor.

combustor. The objective was to obtain the time-averaged velocity data and the combustion-generated soot concentrations, along with primary soot size, at three global fuel-air equivalence ratios (ϕ). The velocity measurements were conducted using the SPIV technique, whereas the soot concentrations and primary soot particle sizes were inferred from the LII measurements. The time-averaged velocity field characteristics and the turbulence intensity profiles as well as the time-averaged soot concentrations and the primary particle diameters of soot for the three cases are presented and discussed. The uncertainties in the velocity and the soot measurements have been quantified and their implications are discussed.

2. Experimental methodology

2.1. Gas turbine model combustor

The gas turbine model combustor used in the current work is shown in Fig. 1. The combustor features a plenum housing the air and fuel delivery systems, and a fused-silica glass enclosure of dimensions 94 × 94 × 114 mm³. The glass enclosure allows optical access into the flame, thereby permitting the utilization of non-intrusive diagnostics for data acquisition. The fuel is supplied through a 6 mm circular nozzle, positioned concentric with the combustor axis. A 12-vane radial swirler, situated inside the combustor plenum, imparts a tangential (swirl) velocity to the inflowing air stream; this swirling jet of air exits through an air nozzle that is concentric with the fuel nozzle and has an outer diameter of 27.85 mm. The exit planes of the fuel and air nozzles are co-

Table 1
Experimental test flow conditions.

Test case	Air flow rate [g/s]	Fuel flow rate [mg/s]	ϕ
1	3.44	52	0.22
2	3.65	52	0.21
3	3.89	52	0.20

ϕ = Global fuel-air equivalence ratio.

planar and the resulting swirl number was measured as 0.55.

It should be noted that, unlike full-scale gas turbine engine combustors, the model combustor used in this work has a square cross-section. The square cross-section leads to characteristic corner vortices or recirculation zones, which provide a virtual cylindrical boundary for the flow [27]. This implies that the flow physics learnt from square cross-section combustors can be extended to real gas turbine combustors with minimal effort. Furthermore, square cross-sections allow an inexpensive design and manufacturing, as well as an easy implementation of laser diagnostics. For the above reasons, a square-cross section model gas turbine combustor was utilized for the current investigation on sooting turbulent swirl flames.

2.2. Experimental test flow conditions

The air and fuel flow conditions used in this work are listed in Table 1. The air and fuel flow rates were chosen to ensure the feasibility of successful SPIV and LII measurements. It was found that flames globally richer than case 1 ($\phi > 0.22$) were very luminous (sooty) and hence, suitable for the LII experiment. However, the high flame luminosity hinders velocity measurements using CCD cameras as will be further discussed in SPIV experimental methodology section. Further, flames globally leaner than case 3 ($\phi < 0.20$) were suitable for SPIV measurements, but hardly contained any soot to be detected using the LII technique. For these reasons, selected air and fuel flow rates were restricted to 3 flame conditions as shown in Table 1.

2.3. SPIV experiment

The three-component velocity data were acquired using the technique of stereoscopic particle image velocimetry whose principles reported by [28,29]. The hardware needed for this experiment includes a laser and a pair of cameras. The laser (Litron Nano-L-PIV) produces beams of wavelength 532 nm, pulse energy 120 mJ, and a pulse duration of 5 ns. The beam was shaped into a sheet using a set of collimation lenses and the resulting laser sheet had dimensions of about 55×1 mm^2. The laser sheet illuminated the flow seeded with 1 μm titanium dioxide particles. The light scattered by the seed was captured using two CCD cameras. The cameras were installed in a plane perpendicular to the laser sheet. The optical axes of the cameras made about 55° with the combustor axis. Each camera head was equipped with a Scheimpflug adapter that ensured the coincidence of the imaging/focusing plane of the camera with the laser sheet [29]. The final angular arrangement of the cameras, needed for the satisfaction of the Scheimpflug criterion, leads to perspective distortion across the field of view. To correct this perspective distortion, a three-dimensional target (LaVision Type 7), and the software package LaVision Davis 8 were utilized. Further, each camera head was also equipped with a macro lens (Nikkor, $f = 105$ mm), and a bandpass filter of center wavelength 532 nm and 1 nm bandwidth (full width at half maximum, FWHM). The 1 nm bandpass filter curtailed the flame luminosity-based background noise from corrupting the recorded image pairs. The SPIV image pairs were recorded using CCD cameras of resolution 2048×2048 pixel^2. The CCD camera shutter stays open after the second laser pulse, and until the start of the next laser pulse pair. For this reason, the second frame of the SPIV image pairs tends to overexpose due to the flame

luminosity, in addition to the background Gaussian noise. The 1 nm bandpass filters, as explained above, play an essential role in successful flow field measurements in sooting turbulent flames.

The SPIV experiment for each flow condition was conducted at 6 Hz, and a total of 2000 image pairs were recorded. The low data acquisition rate posed a challenge of combustor window contamination due to seed deposition. The seed accumulation on the combustor windows leads to diffused illumination of the seeded flow, trapping of seed-scattered light, and stationary spot generation in the SPIV images [26]. To avoid such complications, the 2000 images were recorded over 4 runs, consisting of 500 image pairs each. The SPIV images were processed for velocity vectors in a commercial software package (LaVision Davis 8) using a multi-step algorithm: the interrogation box size was reduced from 64×64 to 32×32 pixel^2, while maintaining an overlap of 50%. The resulting vector fields were post-processed for outliers using the peak search criterion and universal outlier detection. The erroneous vectors were either replaced using vectors corresponding to the second, third or fourth correlation peak in the interrogation box of interest. All other gaps resulting from the failure of the correlation analysis of certain interrogation boxes were filled using spatially (local) interpolated vectors. The final vector fields thus obtained had a vector spacing of 0.78 mm, pertaining to an interrogation box size of 1.56 mm. Further, the uncertainty associated with the mean values reported for the different velocity components varies spatially. To quote a single 95% confidence interval for each component's uncertainty, the flow field location with the longest interval accounts for the worst-case scenario and is therefore chosen as representative of all the flow field locations. Across the test cases, the 95% confidence intervals associated with the uncertainty in the mean radial, axial and tangential velocities are about $\pm$ 0.09 m/s, $\pm$ 0.11 m/s, and $\pm$ 0.08 m/s, respectively.

2.4. LII experiment

The time-averaged soot volume fractions and primary particle diameters were measured using the LII diagnostic technique [30,31]. The experimental components can be grouped under two headings: excitation and detection. The excitation hardware includes a laser, laser beam energy control optics and laser beam shaping optics. The laser (Continuum SLI-10) produced laser beams of wavelength 1064 nm and pulse energy 200 mJ, at a repetition frequency of 10 Hz. The energy of the laser beams was controlled using a half wave plate and a thin film polarizer. Laser fluence was 0.3 J/m^2. It should be noted that laser beams of appropriate energy level (laser fluence) cause minimal soot sublimation during the incandescence excitation step, thereby preserving the non-intrusive character of the LII experiment [32]. Further, the laser beams were shaped into a sheet of dimensions 3 mm $\times$ 100 μm, and subsequently focused at a point in the flame using a slit-relay lens combination. The short-lived soot incandescence thus generated, was collected and recorded using the detection optics. A slit-relay lens combination, identical to that used on the excitation side, collected the incandescent signal from the region of interest in the flame. The collected signal was passed through a dichroic filter, which reflected all wavelengths above 488 nm, while transmitting the remainder of the incident beam. The resulting multi-wavelength beams were focused onto two photo-multiplier tubes (PMT), via achromatic lenses and bandpass filters. The bandpass filters had a center wavelength of 440 nm and 692 nm, respectively and a 40 nm FWHM bandwidth. The incandescence data collected at the two wavelengths allow the application of two-color optical pyrometry for the computation of soot temperature (T_p). The T_p information is essential to calculating the soot volume fraction f_v, and primary particle diameter d_p, at the measurement location in the flame.

The light intensity-voltage calibration of each PMT was performed using an integration sphere unit (Sphere Optics) and a spectrometer. Further, the LII signals collected from the PMTs were processed for the information on T_p, f_v, and d_p, according to the algorithm reported by

Snelling et al. [30].

A laser pulse shot into a turbulent sooting flame may or may not translate into a recorded LII signal due to the intermittency of soot processes. The intermittency of soot processes in turbulent flames is guided by the complex turbulence-chemistry interactions that dominate the turbulent flames [11,14,15]. For this reason, a measurement location in the flow field will have soot occasionally. Further, an LII signal will be recorded when there is a temporal coincidence of the instances when a laser excitation pulse is available, and soot agglomerate(s) occupies the measurement location. Therefore, it is evident that the low probability of recording an LII signal leads to a considerably longer experimental run time. In the current work, the run time for all locations was set to 20 min. Additionally, it was found that about 50 signals were needed for the convergence (± 5%) of the mean f_v and d_p values obtained from the LII signal processing. For this reason, locations showing less than 50 recorded signals over 20 min of run time, were tagged as locations with zero time-averaged soot volume fraction.

3. Results and discussion

3.1. Velocity field measurements

The three-component time-averaged velocity fields for all the three flow conditions are shown in Fig. 2(a)–(c). The three flow fields show similar characteristics: a region of high velocity swirled inflow and two large recirculation zones. The inner recirculation zone (IRZ) surrounds the combustor axis; the boundary of the IRZ is identified as the zero-mean axial velocity curve. The contour plot of the tangential velocity in these figures show that the fluid in the interior of the IRZ has the same sense of rotation about the combustor axis as the main inlet flow. The outer recirculation zone (ORZ) occupies the regions near the combustor windows and shrinks radially with increasing axial height. The ORZ boundary is defined as the zero-mean radial velocity curve. Further, the spatial profiles of local mean velocity magnitude $|\overrightarrow{V_m}|$, turbulence

kinetic energy k, and the turbulence intensity $\sqrt{k}/|\overrightarrow{V_m}|$ for the test case 2 are shown in Fig. 2(d), 3(a) and (b) respectively. Here,

$$|\overrightarrow{V_m}| = \sqrt{\overline{V}_x^2 + \overline{V}_y^2 + \overline{V}_z^2} \tag{1}$$

$$k = \frac{1}{2}(\overline{v_x'^2} + \overline{v_y'^2} + \overline{v_z'^2}) \tag{2}$$

where $\overline{V_i}$ and v_i' represent the time-averaged speed and the root-mean-square of the turbulent velocity fluctuations along the coordinate axis i, respectively. The mean flow velocity magnitude as well as the turbulence kinetic energy peaks in the region exterior to the recirculation zones. Additionally, using Eqs. ((1) and (2)), it can be shown that the recirculation zone boundaries display large values of k but low magnitudes of $|\overrightarrow{V_m}|$. For this reason, the recirculation zone boundaries show turbulence intensity ($\sqrt{k}/|\overrightarrow{V_m}|$) levels exceeding 200%, Fig. 3(b). The high turbulence intensity drives the rapid mixing of cold reactants and hot recirculating fluid near the IRZ boundary, which is critical to the convenient reactant mixture ignition and the consequent flame stabilization in swirl-stabilized combustion systems over a wide range of operating conditions [11,17,19].

3.2. LII measurements

The velocity field measurements indicated that the flow field within the combustor can be assumed to be axisymmetric for the purposes of the current study. For this reason, the soot measurements spanned only one-half of the width of the combustor. The spatial profiles of time-averaged soot concentrations measured in the test case 1 are shown in Fig. 4(a) and (b), while those of the test case 2 are depicted in Fig. 4(c) and (d). The primary particle diameters for test case 1 are shown in Fig. 5. Most of the particle diameters are in the range of 30 to 50 nm. It should be noted here that the lines joining the markers are for visual aid and do not depict any trends regarding the soot concentrations. In the test case 1, for axial heights smaller than 10 mm, most of the soot
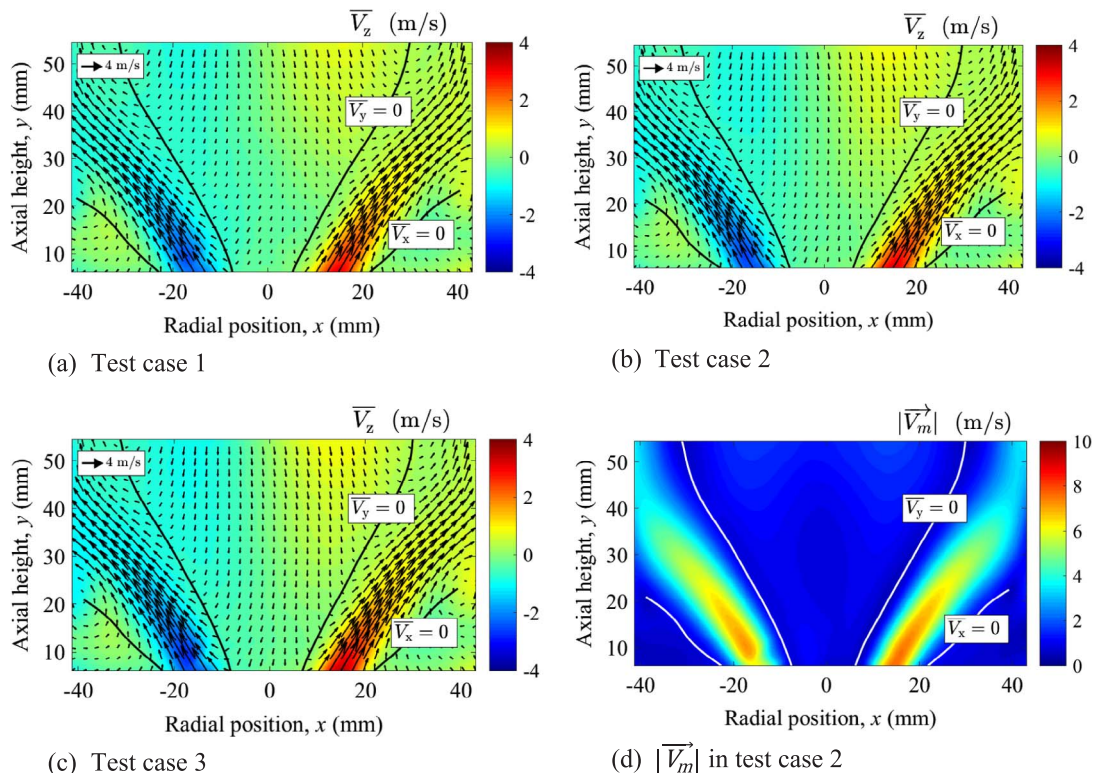

(a) Test case 1

(b) Test case 2

(c) Test case 3

(d) $|\overrightarrow{V_m}|$ in test case 2

Fig. 2. Vector plot of mean axial and radial velocities, overlaid on the contour plot of mean tangential velocity for the test cases 1, 2, and 3, are shown in (a), (b) and (c) respectively. Spatial profile of local mean flow velocity magnitude in test case 3 is shown in (d). The dark/white lines in these plots denote the recirculation zone boundaries.
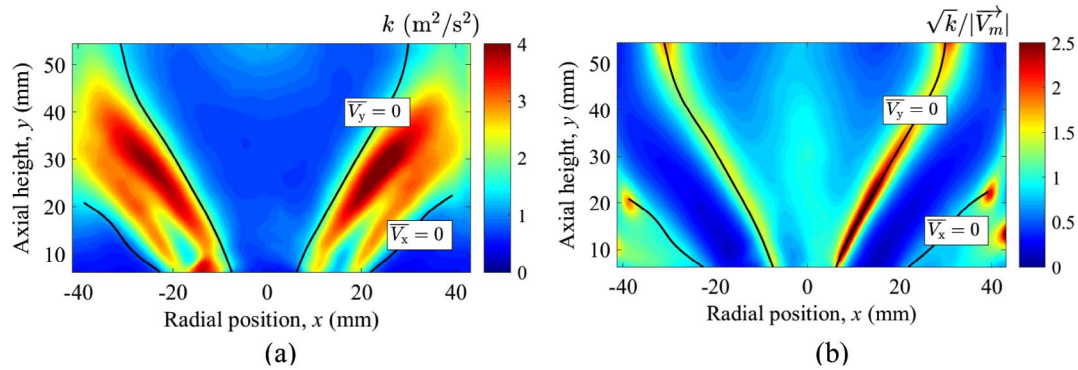
Fig. 3. (a) Turbulence kinetic energy k, and (b) turbulence intensity $\sqrt{k}/|\vec{V_m}|$ profiles for test case 2. The dark lines represent the recirculation zone boundaries.

concentrations is found near the combustor axis and the peak time-averaged soot concentration is about 32 ppb, Fig. 4(a) and (b). With increasing downstream locations, the radial locations with peak soot volume fraction increasingly shift away from the combustor axis. Additionally, the radial locations between the combustor axis and the positions of peak soot concentrations show an increasing presence of soot with increasing downstream locations. At the axial height of 25 mm, the time-averaged soot concentration is almost constant within the radius of 20 mm; beyond this height, the radial soot profiles depict a bimodal character with one of the peaks near the combustor axis. Further, for axial heights above 35 mm, all locations show a decrease in time-averaged soot concentrations with increasing axial height.

Comparison of the soot measurements between test case 1 and 2 highlights the effect of increased air flow rate on the time-averaged soot

concentrations in these flames. A relatively small 6% increase in air flow rate from test case 1 to 2 results in about 50% reduction in the time-averaged soot volume fractions at all measurement locations, see Fig. 4(c) and (d). Between test case 2 and 3, a similar decline in time-averaged soot concentrations is observed as a result of a 6% increase in air flow rate. The peak soot concentration of about 14 ppb in test case 2 reduces to about 8 ppb in test case 3 (not shown). Several measurement locations in test case 3 produced very few LII signals during the data acquisition period; therefore, these locations are assumed to have no statistically significant soot concentrations.

3.3. Uncertainty in LII measurements

The algorithm used to process LII data contains parameters whose
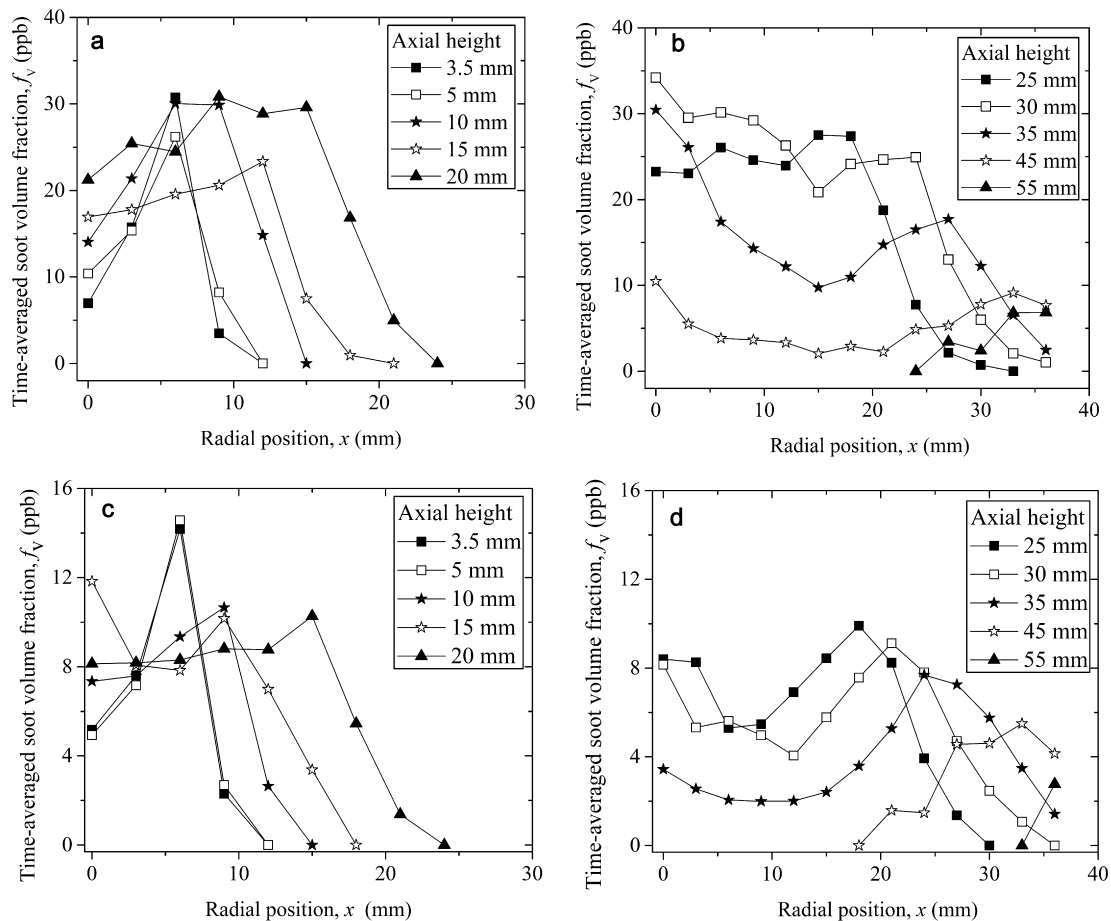

Fig. 4. Time-averaged soot concentration profiles for test case 1 are shown in (a) and (b), whereas those for case 2 are displayed in (c) and (d). Lines through the symbols are provided to guide the eye.
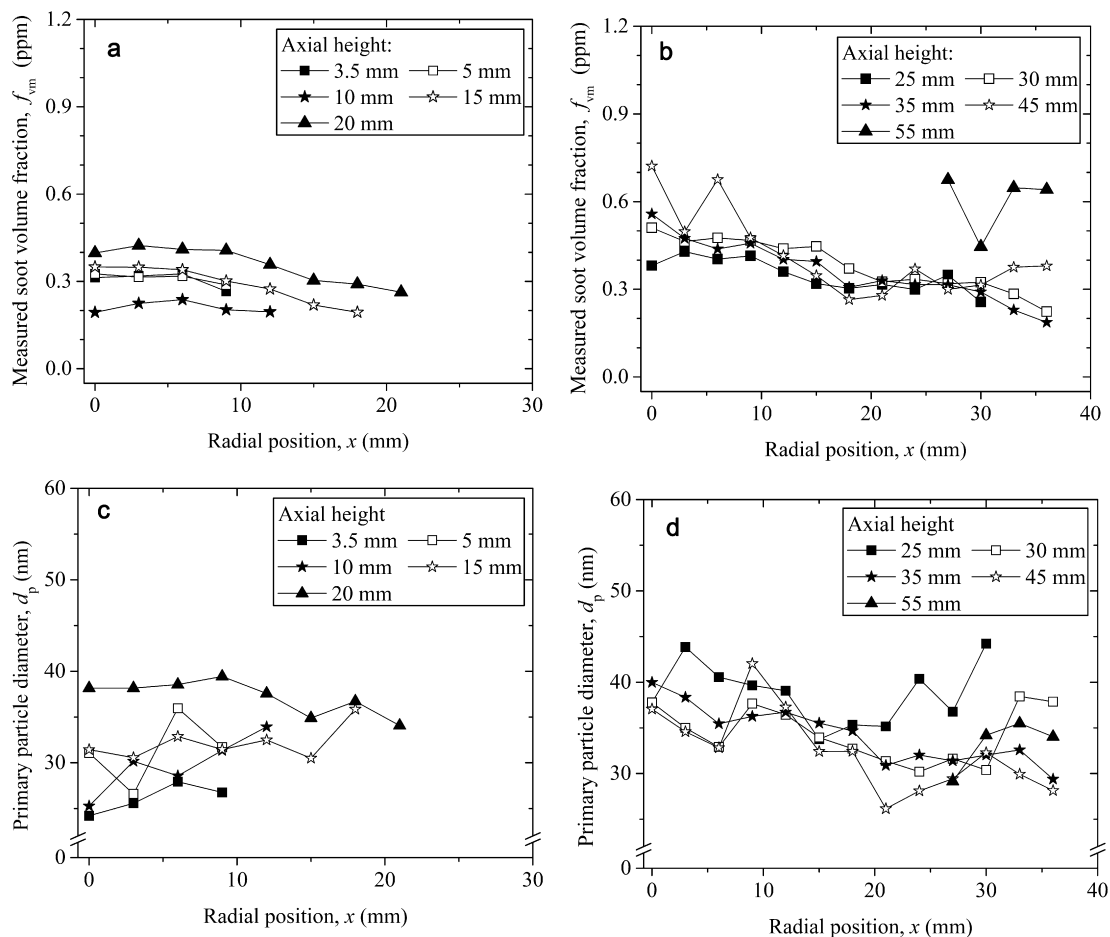
Fig. 5. Radial profiles of measured soot volume fraction profiles (a & b) and primary particle diameters (c & d) in test case 1. Lines through the symbols are provided to guide the eye.

values are either not known with certainty or are prone to fluctuations during the LII experiment [30,33,34]. The propagation of uncertainty of the parameters through to the final soot volume fractions were estimated using a Monte Carlo simulation [34]. In the current work, the parameters include the voltage response of the PMTs, PMT gain voltages, the spectral radiance of integration sphere, soot absorption function values at two measurement wavelengths (440 nm and 692 nm), thermal accommodation coefficient, soot density and ambient gas temperature. An appropriate probability distribution was chosen for each parameter and values were randomly drawn from this distribution. The randomly chosen value for each parameter was used for computing the soot concentrations from the LII signals. This process was repeated several times to obtain a distribution of soot concentration values for various parameter values. Subsequently, the probability distribution of soot values was utilized to compute the 95% confidence interval associated with the reported soot volume fractions [34]. It should be noted that the soot measurements presented above utilize a soot absorption coefficient and thermal accommodation coefficient values of 0.25 and 0.3 respectively.

LII signals were collected from a point in the flame field with the coordinates ($x = 18$ mm, $y = 25$ mm) in test flow condition 1. The time-averaged and measured soot values for this point are plotted in Fig. 4(b) and 5(b) respectively. The LII signals, thus collected, were grouped into batches of 10 signals and averaged for noise reduction. Subsequently, each averaged signal was used for Monte Carlo simulations of the measured soot value. The resulting distributions from each LII averaged signal showed a log-normal shape. Because of its asymmetry about the mean, the 2.5th and 97.5th percentiles were utilized for defining the 95% confidence interval for the systematic uncertainty associated with measured soot concentration obtained from

each averaged LII signal. Additionally, the LII signals were processed for a fixed set of parameter values and the resulting soot concentration was used for the random uncertainty quantification of the measured soot values. The overall uncertainty was computed from the systematic and random uncertainty related to each averaged LII signal, and the longest confidence interval was chosen to encompass all possible soot value in the combustor flame field. The final 95% confidence interval for measured soot concentration spanned from −55% to +84% about the mean value of 0.40 ppm. On the other hand, the primary particle diameter distribution resembled a Gaussian shape. Hence the corresponding 95% confidence interval was found to span ± 45% about the mean value of 35 nm.

3.4. Correlating flow field and soot concentrations

Turbulence intensity along with time-averaged soot concentration and primary particle diameter at an axial height of 25 mm are shown in Fig. 6(a) and (b), respectively. The figures clearly show that soot is mostly found in the interior of the IRZ, the boundary of which follows the peak soot concentration. Additionally, the IRZ boundary also contains the peak turbulence intensities, which is a result of considerable velocity fluctuations but low mean velocity magnitudes. The ignition of reactants happens near the IRZ boundary. In addition to being a site of chemical reactions, the low mean velocity magnitude near the IRZ boundary provides appropriate chemical kinetic time scales needed for soot formation reactions. Hence, it is expected that near the IRZ boundary the soot formation process exceeds the soot oxidation reactions. However, the soot oxidation reactions near the IRZ boundary seem to diminish the primary particle diameters, as shown in Fig. 6(b). Hence, it is expected that an abundance of small primary particles
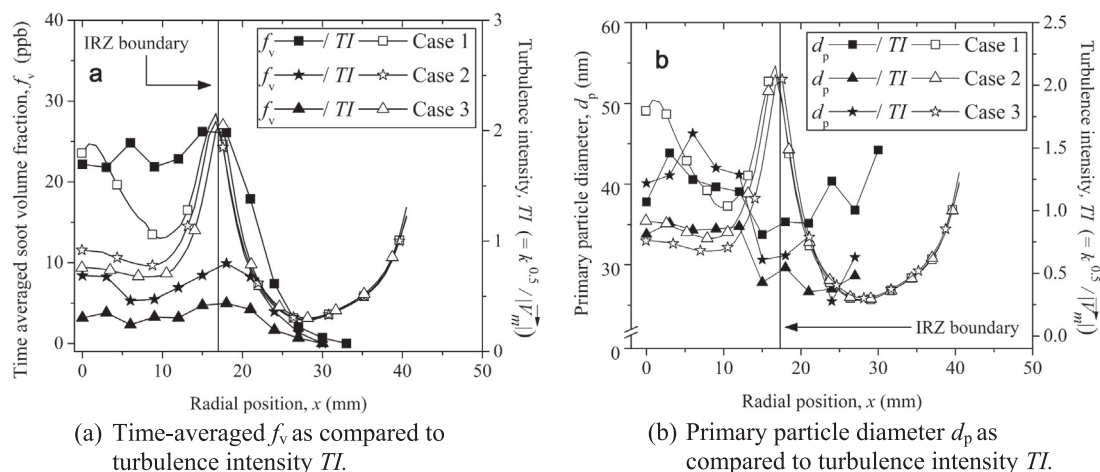
(a) Time-averaged f_v as compared to turbulence intensity *TI*.

(b) Primary particle diameter d_p as compared to turbulence intensity *TI*.

Fig. 6. Radial profiles of turbulence intensity plotted along with (a) time-averaged soot concentration, and (b) primary particle diameter at an axial height of $y = 25\,mm$. The dark vertical line shows the IRZ boundary location at this axial height. Note that turbulence intensity is abbreviated as *TI*.

(compared to the rest of the flow field) produces a peak in the time-averaged soot profile near the IRZ boundary.

When the air flow rate is increased, the local mean velocity magnitude in the entire flow field increases. The higher mean flow speed shortens the flow time available for the soot processes near the IRZ boundary. Additionally, it is documented in the literature that for a fixed fuel jet momentum, higher air flow rates strengthen the turbulent mixing rates [2–4]. The higher mean flow speeds and enhanced turbulent transport processes near the IRZ boundary suppress the soot formation reactions and enhance soot oxidation, similar to the discussion in [14,15] but for turbulent non-premixed jet flames. Reduced soot formation and increased soot oxidation contributes to the intermittency of soot events in the flow field. The combined effect is observed as the significant reduction in the probability of detecting soot in the entire flow field, including the IRZ boundary, for a relatively small increase in the air flow rate. This argument is supported by the observation that primary particle diameters decrease near the IRZ boundary, and this reduction in diameter is larger at higher air flow rates, see Fig. 6(b).

The high intensity turbulent mixing processes near the IRZ boundary transport the soot agglomerates to the interior of the IRZ. Inside the IRZ, the soot faces the oxidative attack of the hot reaction intermediates like OH. Soot particles surviving this oxidation can eventually be transported to the combustor axis. Since the IRZ structure is near-conical, an axisymmetric transport of soot towards the combustor axis is possible. Additionally, the turbulence intensity in the IRZ interior decreases with downstream locations, as shown in Fig. 3(b). Hence, the chance of soot oxidation can be expected to fall with downstream locations, thereby allowing more soot agglomerates to accumulate near the combustor axis. This argument explains the peak near the combustor axis in the time-averaged soot profiles for axial heights below 25 mm, Fig. 4(b). However, for axial heights above 25 mm, it seems that the soot particles must cover the considerable radial width of the IRZ to reach the combustor axis. During the radially-inward transport in the highly turbulent IRZ flow field, majority of the soot agglomerates can be completely oxidized before reaching the combustor axis. For this reason, at axial heights above 25 mm, the time-averaged soot values at the combustor axis decrease with downstream locations, Fig. 4(b) and (d). Nevertheless, for this axial height range, the axisymmetric transport of soot particles from the IRZ boundary creates a peak value at the combustor axis, Fig. 4(b) and (d). Note that the measured soot values increase monotonically with downstream locations, thereby indicating that the large soot agglomerates which survive the oxidative attack of OH radicals in the IRZ can reach the combustor axis, Fig. 5(a) and (b). For axial heights above 40 mm, apparently most of the time-averaged soot is spatially confined to the location of the IRZ

boundary. The combustor axis vicinity becomes increasingly soot-free with downstream heights for axial locations of 40 mm and above, Fig. 4(b) and (c).

4. Concluding remarks

Swirl-stabilized turbulent non-premixed ethylene-air flames were established in a gas turbine model combustor. The three-dimensional velocity field was measured using stereoscopic particle image velocimetry and the time-averaged soot concentrations and primary soot particle diameters were measured using laser induced incandescence. These experiments were conducted separately, but under identical flow conditions. Velocity and soot measurements were performed at three global equivalence ratios. The velocity data captured the recirculation zones separated by a zone of high velocity swirled inflow. The boundaries of the recirculation zones showed high turbulence intensities. Most of the soot was confined to the inner recirculation zone, and the regions having maximum time-averaged soot concentrations grew radially outward with increasing axial height. The time-averaged soot concentrations showed significant reductions with small increases in air flow rate. The intermittency of soot events at the measurement locations in the flame shaped the time-averaged soot profiles, rather than the measured instantaneous soot values. The inner recirculation zone boundary served as the location for the peak time-averaged soot volume fractions at almost all axial heights and for all flow conditions. The primary soot particle diameters derived from laser induced incandescence measurements covered a range from 30 to 50 nm.

Conflict of interest

None

References

[1] N. Syred, N.A. Chigier, J.M. Beér, Flame stabilization in recirculation zones of jets with swirl, Proc. Comb. Inst. 13 (1971) 617–624.
[2] A.K. Gupta, D.G. Lilley, N. Syred, Swirl Flows, Abacus Press, 1984.
[3] N. Syred, J.M. Beér, Combustion in swirling flows: a review, Combust. Flame 23 (1974) 143–201.
[4] B. Janus, A. Dreizler, J. Janicka, Experiments on swirl stabilized non-premixed natural gas flames in a model gas turbine combustor, Proc. Comb. Inst. 31 (2007)

3091–3098.

[5] W. Meier, P. Weigand, X.R. Duan, R. Giezendanner-Thoben, Detailed characterization of the dynamics of the thermo-acoustic pulsations in a lean premixed swirl flame, Combust. Flame 150 (2007) 2–26.

[6] R.H. Chen, J.F. Driscoll, The role of recirculating vortex in improving fuel-air mixing within swirling flows, Proc. Comb. Inst. 22 (1988) 531–540.

[7] D.W. Dockery, C.A. Pope, Acute respiratory effects of particulate air pollution, Annu. Rev. Public Health 15 (1994) 107–132.

[8] S.Y. Lee, S.R. Turns, R.J. Santoro, Measurements of soot, OH and PAH concentrations in turbulent ethylene/air jet flames, Combust. Flame 156 (2009) 2264–2275.

[9] M. Köhler, K.P. Geigle, W. Meier, B.M. Crosland, K.A. Thomson, K. A., G. J. Smallwood, Sooting turbulent jet flame: characterisation and quantitative soot measurements, Appl. Phys. B: Lasers Opt. 104 (2011) 409–425.

[10] M. Köhler, K.P. Geigle, T. Blacha, P. Gerlinger, W. Meier, Experimental characterization and numerical simulation of a sooting lifted turbulent jet diffusion flame, Combust. Flame 159 (2012) 2620–2635.

[11] K.P. Geigle, J. Zerbs, M. Köhler, M. Stöhr, W. Meier, Experimental analysis of soot formation and oxidation in a gas turbine model combustor using laser diagnostics, J. Eng. Gas Turbines Power 133 (2011) 121503-1–121503-9.

[12] K.P. Geigle, R. Hadef, W. Meier, Soot formation and flame characterization of an aero-engine model combustor burning ethylene at elevated pressure, J. Eng. Gas Turbines Power 136 (2014) 021505-1–021505-7.

[13] A. Ruggles, J. Kelman, A gas turbine combustor for instability research and LES validation: Methods and mean results, Combust. Sci. Tech. 186 (2014) 313–331.

[14] N.H. Qamar, Z.T. Alwahabi, Q.N. Chan, G.J. Nathan, D. Roekaerts, K.D. King, Soot volume fraction in a piloted turbulent jet non-premixed flame of natural gas, Combust. Flame 156 (2009) 1339–1347.

[15] N.H. Qamar, G.J. Nathan, Z.T. Alwahabi, K.D. King, The effect of global mixing on soot volume fraction: measurements in simple jet, precessing jet, and bluff body flames, Proc. Comb. Inst. 30 (2005) 1493–1500.

[16] O. Keck, W. Meier, W. Stricker, M. Aigner, Establishment of a confined swirling natural gas/air flame as a standard flame: temperature and species distributions from laser Raman measurements, Combust. Sci. Tech. 174 (2002) 117–151.

[17] W. Meier, I. Boxx, M. Stöhr, C.D. Carter, Laser based investigations in gas turbine model combustors, Exp. Fluids 49 (2010) 865–882.

[18] I. Boxx, C. Slabaugh, P. Kutne, R.P. Lucht, W. Meier, 3 kHz PIV/OH-PLIF measurements in a gas turbine combustor at elevated Pressure, Proc. Comb. Inst. 35 (2015) 3793–3802.

[19] A.M. Steinberg, I. Boxx, C. Carter, W. Meier, Flow-flame interactions causing acoustically coupled heat release fluctuations in a thermo-acoustically unstable gas turbine model combustor, Combust. Flame 157 (2011) 2250–2266.

[20] P. Weigand, W. Meier, X.R. Duan, W. Stricker, M. Aigner, Investigations of swirl flames in a gas turbine model combustor I: flow field, structures, temperature and species distributions, Combust. Flame 144 (2006) 205–224.

[21] W. Meier, X.R. Duan, P. Weigand, Investigations of swirl flames in a gas turbine model combustor II: turbulence-chemistry interactions, Combust. Flame 144 (2006) 225–236.

[22] C. Willert, M. Jarius, Planar flow field measurements in atmospheric and pressurized combustion chambers, Exp. Fluids 33 (2002) 931–939.

[23] B. Quay, T.W. Lee, T. Ni, R.J. Santoro, Spatially resolved measurements of soot volume fraction using laser induced incandescence, Combust. Flame 97 (1994) 384–392.

[24] V. Narayanaswamy, N.T. Clemens, Simultaneous LII and PIV measurements in the soot formation region of turbulent non-premixed jet flames, Proc. Comb. Inst. 34 (2013) 1455–1463.

[25] J. Zerbs, K.P. Geigle, O. Lammel, J. Hader, R. Stirn, R. Hadef, M. Meier, The influence of wavelength in extinction measurements and beam steering in laser-induced incandescence measurements in sooting flames, Appl. Phys. B: Lasers Opt. 96 (2009) 683–694.

[26] U. Stopper, M. Aigner, W. Meier, R. Sadanandan, M. Stöhr, I.S. Kim, Flow field and combustion characterization of premixed gas turbine flames by planar laser techniques, J. Eng. Gas Turbines Power 131 (2009) 021504-1–021504-8.

[27] V.L. Okulov, V.G. Meledin, I.V. Naumov, Experimental investigation of a swirling flow in a cubic container, Tech. Phys. 48 (2003) 1249–1254.

[28] A. Prasad, Stereoscopic particle image velocimetry, Exp. Fluids 29 (2000) 103–116.

[29] A. Prasad, K. Jensen, Scheimpflug stereocamera for particle image velocimetry in liquid flows, Appl. Opt. 34 (1995) 7092–7099.

[30] D.R. Snelling, G.J. Smallwood, F. Liu, Ö.L. Gülder, W.D. Bachalo, A calibration-independent laser-induced incandescence technique for soot measurement by detecting absolute light intensity, Appl. Opt. 44 (2005) 6773–6785.

[31] F. Migliorini, S. De Iuliis, S. Maffi, G. Zizak, Saturation curves of two-color laser-induced incandescence measurements for the investigation of soot optical properties, Appl. Phys. B: Lasers Opt. 120 (2015) 417–427.

[32] R.L. Vander Wal, K.A. Jensen, Laser induced incandescence: excitation intensity, Appl. Opt. 37 (1998) 1608–1616.

[33] F. Liu, D.R. Snelling, K.A. Thomson, G.J. Smallwood, Sensitivity and relative error analyses of soot temperature and volume fraction determined by two-color LII, Appl. Phys. B: Lasers Opt. 96 (2009) 623–636.

[34] B.M. Crosland, M.R. Johnson, K.A. Thomson, Analysis of uncertainties in instantaneous soot volume fraction measurements using two-dimensional, auto-compensating, laser induced incandescence (2D-AC-LII), Appl. Phys. B: Lasers Opt. 102 (2011) 173–183.